Materials Chemistry and Physics 125 (2011) 838–845

Contents lists available at ScienceDirect

Materials Chemistry and Physics

journal homepage: www.elsevier.com/locate/matchemphys

# A comparative study on reactions of *n*-alkylamines with tungstic acids with various W–O octahedral layers: Novel evidence for the "dissolution–reorganization" mechanism

Deliang Chen[a,b,c,*], Tao Li[a], Li Yin[a], Xianxiang Hou[a], Xiujun Yu[a], Yang Zhang[a], Bingbing Fan[a], Hailong Wang[a], Xinjian Li[b], Rui Zhang[a,d], Tiecui Hou[a], Hongxia Lu[a], Hongliang Xu[a], Jing Sun[c], Lian Gao[c]

[a] School of Materials Science and Engineering, Zhengzhou University, 100 Science Road, Zhengzhou 450001, PR China
[b] School of Physics and Engineering, Zhengzhou University, 100 Science Road, Zhengzhou 450001, PR China
[c] The State Key Laboratory of High Performance Ceramics and Superfine Microstructure, Shanghai Institute of Ceramics, Chinese Academy of Sciences, 1295 Dingxi Road, Shanghai 200050, PR China
[d] Laboratory of Aeronautical Composites, Zhengzhou Institute of Aeronautical Industry Management, University Centre, Zhengdong New District, Zhengzhou 450046, PR China

ARTICLE INFO

*Article history:*
Received 25 June 2010
Received in revised form 27 August 2010
Accepted 18 September 2010

*Keywords:*
Inorganic–organic layered hybrid
Tungstic acids
Multilayers
Crystal growth

ABSTRACT

The aim of this paper was to provide a convincing experimental research to demonstrate a dissolution–reorganization mechanism for the formation of tungstate-based inorganic–organic hybrid nanobelts by comparatively investigating the reaction behaviors of $H_2WO_4$ and $H_2W_2O_7{\cdot}xH_2O$ with *n*-alkylamines ($C_mH_{2m+1}NH_2$, $m = 4$–10). The formation of tungstate-based hybrid nanobelts derived from the reactions between *n*-alkylamines and $H_2WO_4$ with single-octahedral W–O layers was investigated with a detailed comparison with those between *n*-alkylamines and $H_2W_2O_7{\cdot}xH_2O$ with double-octahedral W–O layers. $H_2WO_4$ and $H_2W_2O_7{\cdot}xH_2O$ reacted with *n*-alkylamines, respectively, in reverse-microemulsion-like media. The obtained products were characterized by XRD, FT-IR, TG–DTA and SEM. The results indicated that the products derived from $H_2WO_4$ and those from $H_2W_2O_7{\cdot}xH_2O$ were similar in compositions, microstructures and morphologies. The structural analysis indicated the products were tungstate-based inorganic–organic hybrid one-dimensional belts with highly ordered lamellar structures by alternately stacking organic *n*-alkylammonium bilayers and inorganic single-octahedral W–O layers. The *n*-alkyl chains in the above hybrid nanobelts from $H_2WO_4$ and $H_2W_2O_7{\cdot}xH_2O$ took on a bilayer arrangement with tilt angles of 65° and 74°, respectively. The similarities in the microstructures of the products from $H_2W_2O_7{\cdot}xH_2O$ and $H_2WO_4$ demonstrated that the double-octahedral W–O layers of $H_2W_2O_7{\cdot}xH_2O$ were decomposed during the reactions. The changes of inorganic W–O layers and the morphologic changes of the tungstic-acid precursors before and after the reactions corroborated the dissolution–reorganization mechanism.



## 1. Introduction

Intercalation chemistry is one of the *Chimie Douce* approaches to construct inorganic–organic hybrid compounds by inserting organic guest species into a layered inorganic compound [1–5]. The resultant hybrid compounds usually integrate the advantages both of the organic guest species and of the inorganic frameworks [6,7]. There have been a great number of reports on how to construct novel materials and structures via intercalation chemistry, and the as-obtained intercalation compounds have wide applications in catalysis, environmental purification, optics and chemical sensors [8–17]. In addition, inorganic–organic hybrids are suitable precursors to produce nanostructures with controllable morphologies and microstructures [18,19].

Tungsten oxide hydrates include $H_2WO_4$ (or $H_2WO_4{\cdot}H_2O$) with single-octahedral W–O layers and $H_2W_2O_7{\cdot}xH_2O$ with double-octahedral W–O layers, both of which can be used as the host compounds for synthesis of inorganic–organic hybrid materials [16,20–23]. $H_2WO_4$ (or $H_2WO_4{\cdot}H_2O$) can be easily purchased. Johnson et al. [20] reported a layered inorganic–organic hybrid of $WO_3C_5H_5N$ derived by heating $H_2WO_4$ with excess pyridine in the presence of molecular sieves at 423 K. $H_2W_2O_7{\cdot}xH_2O$ can be synthesized by selectively leaching $Bi_2O_2$ layers from the cation-deficient Aurivillius phase of $Bi_2W_2O_9$ [24,25]. There are many

* Corresponding author at: School of Materials Science and Engineering, Zhengzhou University, 100 Science Road, Zhengzhou 450001, PR China.
Tel.: +86 371 63818662; fax: +86 371 63818662.
*E-mail addresses:* dlchen@zzu.edu.cn, dlchennano@hotmail.com (D. Chen).

0254-0584/$ – see front matter © 2010 Elsevier B.V. All rights reserved.
doi:10.1016/j.matchemphys.2010.09.039

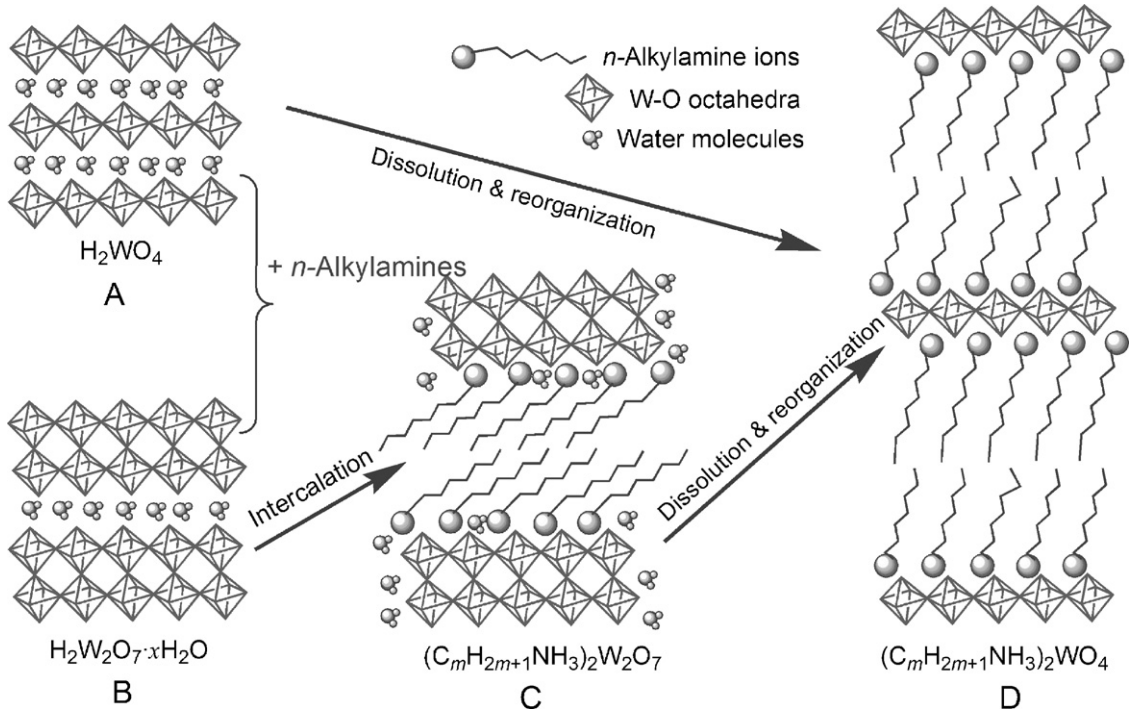


**Fig. 1.** A schematic of the possible mechanisms for the reactions of $H_2W_2O_7{\cdot}xH_2O$ and $H_2WO_4$ with *n*-alkylamines in heptane: (A) $H_2WO_4$ powders with single-octahedral W–O layers, (B) $H_2W_2O_7{\cdot}xH_2O$ powders with double-octahedral W–O layers, (C) intermediate hybrids with double-octahedral W–O layers derived by an intercalation reaction, and (D) tungstate-based inorganic–organic hybrids with single-octahedral W–O layers derived by a dissolution–reorganization process.

reports on the intercalation and exfoliation reactions of layered $H_2W_2O_7{\cdot}xH_2O$ compounds with organic amines. For example, Schaak and Mallouk [25] reported the exfoliation of $H_2W_2O_7$ into $TBA_xH_{2-x}W_2O_7$ nanosheets in a quaternary ammonium hydroxide ($TBA^+OH^-$) aqueous solution. Kudo et al. [24] and Wang et al. [26] reported intercalation reactions of *n*-alkylamines into $H_2W_2O_7{\cdot}xH_2O$ in heptane, and they thought that the *n*-alkylamine molecules were intercalated into the interlayer spaces via an acid-base mechanism and that the as-obtained intercalation compounds kept the double-octahedral W–O layers intact [24–26]. Recently, we also investigated the reaction behaviors of $H_2W_2O_7{\cdot}xH_2O$ with *n*-alkylamines [27,28]. However, our results indicated that the double-octahedral W–O layers from $H_2W_2O_7{\cdot}xH_2O$ were dissolved, and the dissolved species were then reorganized into highly ordered inorganic–organic hybrids with single-octahedral W–O layers, when nonpolar reagents (*e.g.*, heptane, pentane, decane and cyclohexane) were used as the reaction solvents [27,28]. Therefore, there are still confusions about the intercalation chemistry of layered tungstic acids, although they have been intensively investigated recently [24–28].

For the reactions of $H_2W_2O_7{\cdot}xH_2O$ with *n*-alkylamines, one of the confusions is that some researchers have concluded that the double-octahedral W–O layers of $H_2W_2O_7{\cdot}xH_2O$ can be transferred to the final inorganic–organic hybrids via an intercalation reaction [24–26], as shown in Fig. 1B and C, whereas other researchers have obtained evidence that the double-octahedral W–O layers from $H_2W_2O_7{\cdot}xH_2O$ are firstly dissolved and then reorganized to single-octahedral W–O layers during the reactions of $H_2W_2O_7{\cdot}xH_2O$ and *n*-alkylamines in nonpolar solvents [27–32], as shown in Fig. 1B–D. To clarify the above inconsistency, we design a comparative experimental study in this paper, using $H_2W_2O_7{\cdot}xH_2O$ with double-octahedral W–O layers and $H_2WO_4$ with single-octahedral W–O layers as the starting inorganic materials, as shown in Fig. 1. The double-octahedral W–O layers in $H_2W_2O_7{\cdot}xH_2O$ can serve as a kind of identifier. The reactions of $H_2WO_4$ and $H_2W_2O_7{\cdot}xH_2O$ compounds with *n*-alkylamines ($C_mH_{2m+1}NH_2$, $m = 4$, 6, 8 and 10) are conducted under a similar condition in reverse-microemulsion-like media. The compositions, microstructures and morphologies of the resultant products via the reactions of $H_2WO_4$ and $H_2W_2O_7{\cdot}xH_2O$ with *n*-alkylamines are comparatively investigated via X-ray diffraction (XRD), Fourier-transform infrared (FT-IR) spectra, thermal analysis (TG–DTA) and scanning electron microscopy (SEM). By comparing the characteristics of the as-obtained hybrid compounds, we infer the possible reaction process and related mechanisms.

## 2. Materials and methods

### 2.1. Material and chemicals

$H_2WO_4$, $WO_3$, $Bi_2O_3$, hydrochloric acid (HCl) and heptane were purchased from the Sinopharm Chemical Reagent Co., Ltd. The reagents of *n*-alkylamines were purchased from the Aldrich Chemical Company Inc. All chemicals were analytically pure and used as received without further treatment. $H_2W_2O_7{\cdot}xH_2O$ ($x \sim 0.5$–2) was synthesized via a similar process described previously in Refs. [24,29], using a HCl solution to leach the $[Bi_2O_2]$ layers from a layered $Bi_2W_2O_9$ phase, which was prepared through a solid-state reaction of $Bi_2O_3$ powders with $WO_3$ powders at 800 °C [24,29].

### 2.2. Reactions of n-alkylamines with $H_2WO_4$ powders

The reactions of $H_2WO_4$ powders and *n*-alkylamines with various alkyl-chain lengths were conducted using heptane as the solvent via a similar process (Scheme S1) to our previous report [27]. Typically, ~0.3 g (~1.2 mmol) of $H_2WO_4$ powders was dispersed in a mixture of ~1.32 g (~18 mmol) of $C_4H_9NH_2$ and ~15 mL of heptane under an intense stirring condition at room temperature. The stirring was kept on for 10–40 h till the resultant suspension turned to be white in color. The suspension was centrifuged and then washed with ethanol twice, and a white solid was obtained. The solid was air-dried at a reduced pressure at room temperature before used for characterizations. The as-obtained sample with $H_2WO_4$ powders and $C_4H_9NH_2$ was denoted as $C_4N@H_2WO_4$. The molar ratio of $C_4H_9NH_2$ to $H_2WO_4$ was ~15. Similarly, $C_6H_{11}NH_2$, $C_8H_{15}NH_2$ and $C_{10}H_{21}NH_2$ were used as the reactants under the same reaction condition, and the resultant samples were denoted as $C_6N@H_2WO_4$, $C_8N@H_2WO_4$ and $C_{10}N@H_2WO_4$, respectively.

### 2.3. Reactions of n-alkylamines with $H_2W_2O_7{\cdot}xH_2O$ powders

The process for the reactions of $H_2W_2O_7{\cdot}xH_2O$ with *n*-alkylamines ($C_mH_{2m+1}NH_2$, $m = 4$, 6, 8 and10) was similar to that of $H_2WO_4$ with *n*-alkyl-

amines described above (Scheme S1) [27]. The molar ratios of *n*-alkylamines to $H_2W_2O_7{\cdot}xH_2O$ were ~30, and the volume ratios of heptane to *n*-alkylamines were maintained at ~5. Typically, ~0.3 g of the air-dried $H_2W_2O_7{\cdot}xH_2O$ was dispersed in the mixture of heptane and *n*-alkylamine under a magnetic stirring condition. After a reaction for more than 10 h, the products were collected from the suspensions by centrifugation and washed with ethanol. The as-obtained solids were air-dried under a reduced pressure at room temperature. The samples derived from the reactions of $H_2W_2O_7{\cdot}xH_2O$ with $C_4H_9NH_2$, $C_6H_{11}NH_2$, $C_8H_{15}NH_2$ and $C_{10}H_{21}NH_2$ were marked as $C_4N@H_2W_2O_7$, $C_6N@H_2W_2O_7$, $C_8N@H_2W_2O_7$ and $C_{10}N@H_2W_2O_7$, respectively.

### 2.4. Characterization and analysis

The phase compositions of the precursors and the resultant products were determined by X-ray diffraction (XRD; Rigaku D/Max-3B diffractometer with Cu Kα radiation or with Fe Kα radiation). The morphologies of the precursors and the as-obtained products were observed on a scanning electron microscope (SEM, JEOL JSM-5600). Thermal analysis (TG–DTA) was performed using a NETZ SCH Simultaneous Thermal Analyzer with a heating rate of 10 K $min^{-1}$ in an air flow. Fourier-transform infrared (FT-IR) spectra were recorded on a Brucke-VECTOR22 spectrophotometer using a KBr disk technique in the 400–4000 $cm^{-1}$ region. The interlayer distances of the as-obtained hybrids and the cell parameters of the precursors were calculated on the basis of their XRD patterns using a UnitCell program (by TJB Holland and SAT Redfern, 1995) by minimizing the sum of squares of residuals in $2\theta$.

## 3. Results and discussion

### 3.1. Phase compositions and morphologies of tungstic acid precursors

The XRD patterns of the commercially available $H_2WO_4$ powders and the $H_2W_2O_7{\cdot}xH_2O$ powders synthesized by leaching $[Bi_2O_2]$ layers from the layered $Bi_2W_2O_9$ phase [29] were analyzed (Fig. S1). As the results show, the XRD pattern of $H_2W_2O_7{\cdot}xH_2O$ is close to the results reported in Refs. [24,29], and the strong peaks located around 7.90°, 16.0° and 24.1° in $2\theta$ can be indexed to be (0 0 2), (0 0 4) and (0 0 6) reflections, respectively. The calculated cell parameters, according to the XRD data (Fig. S1a) and an orthorhombic crystal system, are $a = 0.521(7)$ nm, $b = 0.518(7)$ nm and $c = 2.23(4)$ nm, which are consistent with the reported values [24,27]. The intense peaks from (0 0 *l*) reflections suggest that the $H_2W_2O_7{\cdot}xH_2O$ precursor is of a typical layered structure, the normal of which is along the [0 0 *l*] direction [24,27]. The XRD pattern (Fig. S1b) of the commercially obtained $H_2WO_4$ powders can be indexed to be tungsten oxide hydrate ($WO_3{\cdot}H_2O$) with an orthorhombic system [S.G.: *Pmnb* (62)] according to the JCPDS card No. 43-0679. The calculated cell parameters are $a = 0.524(2)$ nm, $b = 1.065(5)$ nm and $c = 0.513(2)$ nm by refining the XRD data in an orthorhombic system. These values are very close to the literature data [JCPDS card No. 43-0679, $a = 0.5238(2)$ nm, $b = 1.0704(4)$ nm, $c = 0.5120(2)$ nm]. The normal of the layer structures in $H_2WO_4$ is along the [0 *k* 0] direction according to its XRD pattern.

The morphologies of $H_2WO_4$ and $H_2W_2O_7{\cdot}xH_2O$ powders were observed on SEM and TEM microscopes (Fig. S2). The SEM image indicates that the $H_2WO_4$ powders consist of submicron aggregations, most of which are assemblies of $H_2WO_4$ nanocrystals. The TEM image shows that the commercially available $H_2WO_4$ powders are mainly composed of nanoscale particles and nanosheets, agreeing with the SEM observations (Fig. S2a). The $H_2W_2O_7{\cdot}xH_2O$ powders consist of microscale platelike particles with thicknesses of 1–5 μm, and their side lengths vary from 5 to 20 μm (Fig. S2b). The microscale plates are usually single-crystalline [24,29]. One can find that the morphologies and particle sizes of $H_2W_2O_7{\cdot}xH_2O$ powders are very different from those of $H_2WO_4$ powders.

### 3.2. Reactions of n-alkylamines with $H_2WO_4$ powders and XRD analysis of the resultant hybrids

The reactions of *n*-alkylamines with $H_2WO_4$ powders were carried out in a nonpolar solvent of heptane at room temperature.

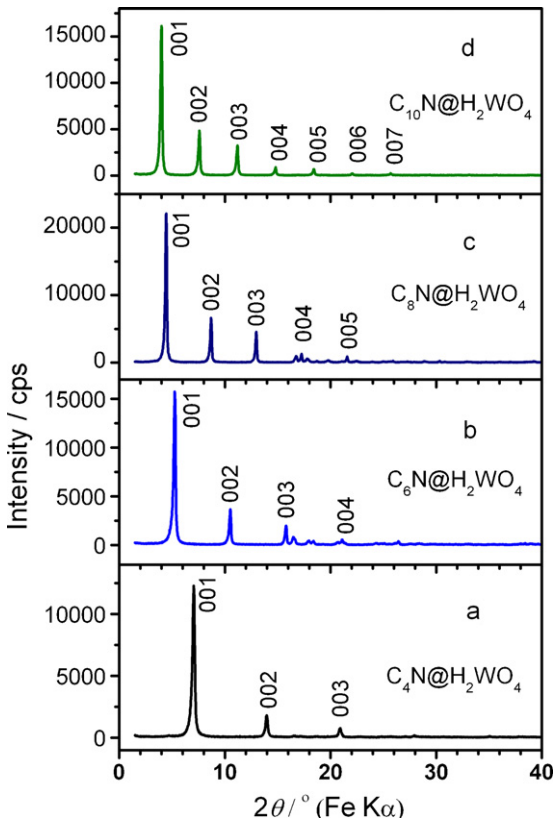


**Fig. 2.** XRD patterns of the tungstate-based hybrid compounds ($C_mN@H_2WO_4$) obtained via reactions between $H_2WO_4$ and *n*-alkylamines in heptane: (a) $C_4N@H_2WO_4$, (b) $C_6N@H_2WO_4$, (c) $C_8N@H_2WO_4$, and (d) $C_{10}N@H_2WO_4$.

Actually, other nonpolar solvents, including hexane and cyclohexane, are also suitable for the reactions *n*-alkylamines with $H_2WO_4$ powders. In the present reactions, *n*-alkylamines not only act as one of the reactants, but also act as a surfactant to form pseudo water-in-oil microemulsions, in which the hydrophilic $H_2WO_4$ particles act as the "water" phase, *i.e.*, $H_2WO_4$/*n*-alkylamine/heptane (hydrophilic phase/surfactant/oil phase) [27]. After the reactions are complete, the resultant suspensions become fully white in color. The molar ratios of *n*-alkylamines to $H_2WO_4$ are kept at about 15, and the volume ratios of heptane to *n*-alkylamines are about 5. For the short alkyl-chain amines of $C_4H_9NH_2$ and $C_6H_{11}NH_2$, the reactions with $H_2WO_4$ particles can be finished in 10 h, whereas the $C_8H_{15}NH_2$ and $C_{10}H_{21}NH_2$ with longer alkyl-chains need more times (about 20 h) to finish their reactions with $H_2WO_4$ particles. When a small amount of water is added to wet $H_2WO_4$ particles before reactions, the reactions between $H_2WO_4$ particles and *n*-alkylamines are obviously accelerated and can be finished in several hours. The ratios of *n*-alkylamines to $H_2WO_4$ also affect the reactions. For example, the reaction between *n*-octylamine and $H_2WO_4$ can be finished in 5 h when the molar ratio of *n*-octylamine to $H_2WO_4$ is larger than 10, whereas the reaction cannot be completed after several days when the *n*-octylamine-to-$H_2WO_4$ ratio is 2. The water amounts and the *n*-octylamine-to-$H_2WO_4$ ratios are therefore the key factors influencing the speed of the reactions between *n*-octylamine and $H_2WO_4$ powders in present conditions.

Fig. 2 shows the typical XRD patterns of the resultant products derived from the reactions of *n*-alkylamines with $H_2WO_4$ powders. One can find that the diffraction peaks belonging to $H_2WO_4$ disappear, and a series of new diffraction peaks in the low $2\theta$ regions occur after the reactions of $H_2WO_4$ with *n*-alkylamines. From several degrees to 30° in $2\theta$, there are several diffraction peaks with regularly reduced intensities, which is the typical characteristic

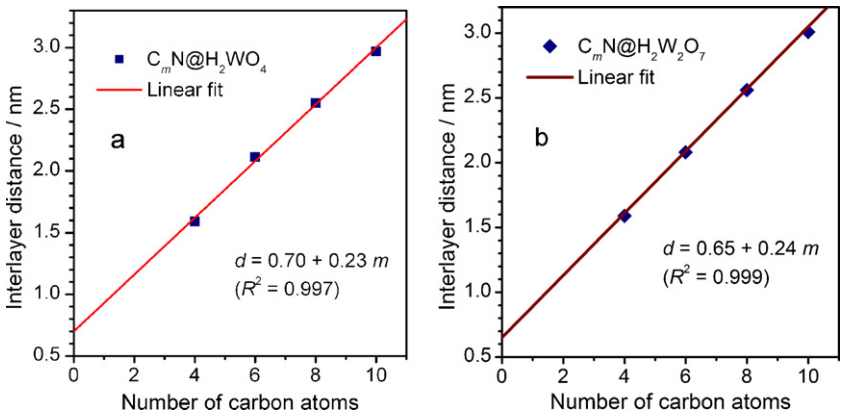


**Fig. 3.** (a) A plot of the interlayer distances of the $C_mN@H_2WO_4$ compounds as a function of the carbon numbers of the corresponding *n*-alkylamines; (b) a plot of the interlayer distances of the $C_mN@H_2W_2O_7$ compounds as a function of the carbon numbers of the corresponding *n*-alkylamines.

of an ordered layered structure [27]. The number of the diffraction peaks of $C_mN@H_2WO_4$ increases as the carbon number of the *n*-alkyl chains increases from 4 to 10. There are 3 perceptible diffraction peaks for $C_4N@H_2WO_4$, whereas there are 7 diffraction peaks for $C_{10}N@H_2WO_4$. The increase in number of the diffraction peaks indicates that the degree of order of the layered $C_mN@H_2WO_4$ structures is improved when the *n*-alkylamines with longer alkyl chains are used. The diffraction peaks can be indexed to the (0 0 *l*) reflections [27].

The interlayer distances of $C_mN@H_2WO_4$ are calculated according to the (0 0 *l*) reflections in their XRD patterns (Fig. 2). The calculated interlayer distances (*d*) of $C_4N@H_2WO_4$, $C_6N@H_2WO_4$, $C_8N@H_2WO_4$ and $C_{10}N@H_2WO_4$ are 1.59(2) nm, 2.112(3) nm, 2.55(7) nm and 2.97(9) nm, respectively. Fig. 3a shows the plot of the interlayer distances (*d*) of the $C_mN@H_2WO_4$ as a function of the carbon numbers of their corresponding *n*-alkylamines. The linear fitting result indicates there is an excellent linear relationship ($R^2$ = 0.997) between the interlayer distances (*d*) and the corresponding alkyl-chain lengths (*m*): $d$ (nm) = 0.70 + 0.23$m$ ($4 \leq m \leq 10$). The slope *k* is 0.23, and its intercept $d_0$ is 0.70 nm at $m$ = 0.

The increment per –$CH_2$– for a fully extended all-trans alkyl chain is 0.127 nm [33]. When $k \leq 0.127$, the arrangement is probably a monolayer with a tilt angle $\alpha$ [$\alpha = \sin^{-1}(k/0.127)$]. When $0.127 < k \leq 0.254$, a bilayer arrangement with a tilt angle of $\alpha = \sin^{-1}(k/0.254)$ is usually considered [34]. In the present case, $0.127 < k = 0.23 < 0.254$, the *n*-alkyl chains in $C_mN@H_2WO_4$ probably take on a bilayer arrangement with a tilt angle of $\alpha = \sin^{-1}(0.23/0.254) = 65^\circ$ along the inorganic layers.

The thickness of the inorganic layers can be estimated by extrapolating the interlayer distance for $m$ = 1 ($d_1$ = 0.93 nm). Since the bond lengths of C–N and N–H in $RNH_2$ are 0.147 and 0.101 nm [35], respectively, the length ($l_1$) of a $CH_3NH_2$ molecule or $CH_3NH_3^+$ ion can be estimated approximately as the sum (0.248 nm) of 0.147 and 0.101 nm [27]. Due to the bilayer arrangement and the tilt angle ($\alpha = 65^\circ$), the contribution of the organic layers ($CH_3NH_2$ molecules or $CH_3NH_3^+$ ions) to the interlayer distance ($d_1$) can be estimated as $h_o = 2l_1 \cdot \sin\alpha$ = 0.45 nm. The thickness of the inorganic layers ($h_i$) can therefore be calculated by subtracting $h_o$ from $d_1$, *i.e.*, $h_i$ = 0.93–0.45 = 0.48 nm. This value (0.48 nm) is close to the thickness (~0.41 nm) of the single-octahedral W–O layer [36].

### 3.3. Reactions of n-alkylamines with $H_2W_2O_7 \cdot xH_2O$ powders and XRD analysis of the resultant hybrids

The process and conditions for the reactions of $H_2W_2O_7 \cdot xH_2O$ powders with *n*-alkylamines are similar to those of $H_2WO_4$, and the detailed information can be referred to the Refs. [27,28]. The molar ratios of *n*-alkylamines to $H_2W_2O_7 \cdot xH_2O$ are about 30. The reactions of $H_2W_2O_7 \cdot xH_2O$ with *n*-alkylamines are rapid, and the suspensions turn to be white after a 6-h reaction for $C_mN@H_2W_2O_7$ compounds ($m$ = 4, 6, 8 and 10).

Fig. 4 shows the typical XRD patterns of $C_mN@H_2W_2O_7$ with $m$ = 4, 6, 8 and 10. There are a series of new diffraction peaks (0 0 *l*) in the low 2$\theta$ region, and the XRD peaks belonging to $H_2W_2O_7 \cdot xH_2O$ disappear. The intensities of the peaks regularly decrease from low values to high values in 2$\theta$, indicating that the as-obtained samples $C_mN@H_2W_2O_7$ are of a highly ordered layered structure. The numbers of the perceptible diffraction peaks increase from 4 for $C_4N@H_2W_2O_7$ to 7 for $C_{10}N@H_2W_2O_7$, suggesting that the degree of order is enhanced for the $C_mN@H_2W_2O_7$ hybrids with longer *n*-alky chains, similar to the case of $C_mN@H_2WO_4$ hybrids (Fig. 2).

The calculated interlayer distances of $C_mN@H_2W_2O_7$ on the basis of their XRD data are 1.59(3) nm, 2.08(4) nm, 2.56(6) nm and 3.01(5) nm for $C_4N@H_2W_2O_7$, $C_6N@H_2W_2O_7$, $C_8N@H_2W_2O_7$ and

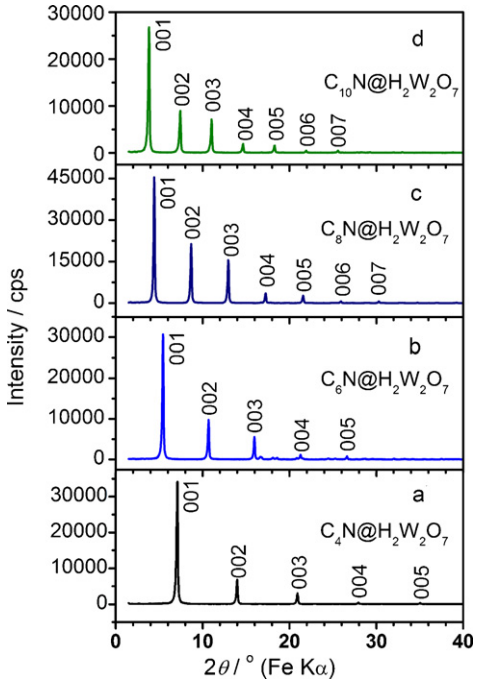


**Fig. 4.** XRD patterns of the $C_mN@H_2W_2O_7$ obtained via reactions between $H_2W_2O_7 \cdot xH_2O$ and *n*-alkylamines in heptane: (a) $C_4N@H_2W_2O_7$, (b) $C_6N@H_2W_2O_7$, (c) $C_8N@H_2W_2O_7$, and (d) $C_{10}N@H_2W_2O_7$.

$C_{10}N@H_2W_2O_7$, respectively. Fig. 3b shows the plot of the interlayer distances ($d$) versus the carbon numbers ($m$) of $n$-alkylamines used. The result of linear fit ($R^2 = 0.999$) is $d$ (nm) = 0.65 + 0.24 $m$ ($4 \leq m \leq 10$). The slope $k$ is 0.24, and its intercept $d_0$ is 0.65 nm at $m = 0$. Similarly, because $0.127 < k = 0.24 < 0.254$, the $n$-alkyl chains in the $C_mN@H_2W_2O_7$ compounds should take on a bilayer arrangement with a tilt angle of $\alpha = \sin^{-1}(0.24/0.254) = 74^\circ$ along the inorganic layers. The thickness of the inorganic layers can also be estimated by extrapolating the interlayer distance for $m = 1$ ($d_1 = 0.89$ nm). According to the previous analysis, the length ($l_1$) of a $CH_3NH_2$ molecule or $CH_3NH_3^+$ ion is about 0.248 nm. Because of the bilayer arrangement and the tilt angle ($\alpha = 74^\circ$), the contribution of the organic layers ($CH_3NH_2$ molecules or $CH_3NH_3^+$ ions) to the interlayer distance ($d_1$) can be estimated as $h_o = 2l_1 \cdot \sin\alpha = 0.48$ nm. Thus the thickness of the inorganic layers ($h_i$) is calculated to be $h_i = 0.89 - 0.48 = 0.41$ nm, which is much less than the thickness (0.93 nm) of the double-octahedral W–O layers, but is close to the thickness of the single-octahedral W–O layers. The above results are in agreement with our previously reported data [27].

When comparing Fig. 2 with Fig. 4, one can find that the XRD patterns of the $C_mN@H_2WO_4$ compounds are very close to those of their corresponding $C_mN@H_2W_2O_7$ compounds, except their intensities. The more intense diffraction peaks of $C_mN@H_2W_2O_7$ than $C_mN@H_2WO_4$ indicate that the former shows a higher degree of order in the layered structure than the latter. From Fig. 3, one can find that the arrangements of $n$-alkyl chains in the $C_mN@H_2WO_4$ and $C_mN@H_2W_2O_7$ compounds are similar to each other, and that thicknesses of the inorganic layers in the $C_mN@H_2WO_4$ and $C_mN@H_2W_2O_7$ compounds are very close to that of the single-octahedral W–O layer.

### 3.4. FT-IR spectra of the hybrids derived from $H_2WO_4$ and $H_2W_2O_7$ powders

The FT-IR spectra (Fig. S3 and Table S1) of the representative samples of $C_8N@H_2WO_4$ and $C_8N@H_2W_2O_7$ indicate that the IR absorption bands of $C_8N@H_2WO_4$ are very close to those of $C_8N@H_2W_2O_7$.

The wide bands at 3432 $cm^{-1}$ are ascribed to the symmetrical stretching vibration of the –OH groups of the absorbed $H_2O$ molecules [$\nu_s$(O–H)]. The bands at 3307 and 3298 $cm^{-1}$ are ascribed to the asymmetrical stretching vibration of the $-NH_2$ group, *i.e.*, $\nu_{as}$(N–H), and those at 3237 and 3231 $cm^{-1}$ are ascribed to the stretching vibration of the $-NH_2$ group, *i.e.*, $\nu_s$(N–H) [37]. The weak bands at 1634 and 1636 $cm^{-1}$ can be ascribed to the bending vibration of the N–H bonds in $-NH_2$ groups, *i.e.*, $\delta$(N–H) [38]. The bands at 1580 and 1576 $cm^{-1}$ can be ascribed to the bending vibration of the N–H bonds in $-NH_3^+$ groups [38]. The bands at 2846 and 2847 $cm^{-1}$ are ascribed to the symmetrical stretching vibration of the C–H bonds in the $-CH_2-$ groups, and those at 2925 and 2918 $cm^{-1}$ are ascribed to the asymmetrical stretching vibration of the C–H bonds in the $-CH_2-$ groups [39,40]. The bands at 756 and 756 $cm^{-1}$ are ascribed the out-of-plane rocking vibration of the $-CH_2-$ group, *i.e.*, $\gamma$(C–H) [41]. The bands at 2960 $cm^{-1}$ and 2957 $cm^{-1}$ are ascribed to symmetrical stretching vibration of the C–H bonds in the $-CH_3$ groups [39,40]. The bands at 1395 and 1393 $cm^{-1}$ are ascribed to the deformation vibration of $-CH_3$, *i.e.*, $\delta_s$(C–H) [41]. The bands at 1467 $cm^{-1}$ are ascribed to the asymmetrical stretching vibration of the C–H bonds in the $-CH_3$ and $-CH_2-$ groups, *i.e.*, $\delta_{as}$(C–H) [41]. The bands at 1057 and 1055 $cm^{-1}$ are ascribed to symmetrical stretching vibration of the C–N bonds in the $\equiv C-NH_2$ groups, *i.e.*, $\nu_s$(C–N) [41].

The bands at 564 and 560 $cm^{-1}$ are ascribed $\nu$(W–O–W) due to the corner-sharing $WO_6$ units [38], and the bands at 905 $cm^{-1}$ and 865 $cm^{-1}$ can be assigned to the vibration of $\nu$(W=O) [38]. The wide bands around at 2100 $cm^{-1}$ are ascribed to the combination of the symmetrical vibration [$\nu_{as}(-NH_3^+)$] and the torsion oscillation [$\tau(-NH_3^+)$] of the $-NH_3^+$ group, which interacts with the apical oxygen of the W–O framework, *i.e.*, $[-NH_3]^+\cdots^-$[O–W–O] [26,27,38]. The FT-IR results indicate that the obtained $C_8N@H_2WO_4$ and $C_8N@H_2W_2O_7$ have a similar inorganic-organic hybrid structure.

### 3.5. Morphologies of the hybrids derived from $H_2WO_4$ and $H_2W_2O_7$ powders

Fig. 5a–d shows the typical SEM images of the resultant inorganic–organic hybrid compounds of $C_mN@H_2WO_4$ ($m = 4$, 6, 8 and 10). For sample $C_4N@H_2WO_4$, one-dimensional morphology can be discernable but not uniform, and their length-to-diameter ratios are small (Fig. 5a). For samples $C_6N@H_2WO_4$, $C_8N@H_2WO_4$ and $C_{10}N@H_2WO_4$, the one-dimensional morphologies become more definite and more uniform than those of $C_4N@H_2WO_4$ (Fig. 5b–d). In particular, the hybrid of $C_8N@H_2WO_4$ has more typically one-dimensional shapes with a length-to-diameter ratio region of 5–15 (Fig. 5c), and their apparent diameters are about 300 nm. It can be found that the dimensions of $C_6N@H_2WO_4$ and $C_{10}N@H_2WO_4$ are smaller than those of $C_8N@H_2WO_4$, when we compare Fig. 5b–d.

For purposes of comparison, we also show typical SEM images of $C_mN@H_2W_2O_7$ hybrids ($m = 4$, 6, 8 and 10) in Fig. 5e–h. One can see that all the samples, including $C_4N@H_2W_2O_7$, $C_6N@H_2W_2O_7$, $C_8N@H_2W_2O_7$ and $C_{10}N@H_2W_2O_7$, take on a definite one-dimensional structure, with a length region of 20–50 μm. Their apparent diameters are about 200–500 nm according to the previously reported data [27,28].

When comparing the morphologies in Fig. 5, one can find that the one-dimensional morphologies of the $C_mN@H_2W_2O_7$ hybrids are more uniform and definite than those of the $C_mN@H_2WO_4$ hybrids. Also, the length-to-diameter ratios of $C_mN@H_2W_2O_7$ hybrids are larger than those of $C_mN@H_2WO_4$ hybrids. The difference in morphology between the $C_mN@H_2WO_4$ and $C_mN@H_2W_2O_7$ hybrids may be due to the difference in size and morphology between their precursors, *i.e.*, $H_2WO_4$ and $H_2W_2O_7 \cdot xH_2O$. As shown in Fig. S2, $H_2W_2O_7 \cdot xH_2O$ has larger particle sizes than $H_2WO_4$, and each $H_2W_2O_7 \cdot xH_2O$ particle is single-crystalline, whereas the $H_2WO_4$ particles are aggregates of small nanocrystals. The larger size and the more highly crystallized phase may facilitate to form more highly ordered and uniform inorganic–organic hybrid compounds. Also, the double-octahedral W–O lamellar structure in $H_2W_2O_7 \cdot xH_2O$ is more favorable to form highly ordered and uniform inorganic–organic hybrid compounds than $H_2WO_4$ with a single-octahedral W–O lamellar structure. The enhanced degree of order in the microstructures of $C_mN@H_2W_2O_7$ hybrids can also be concluded according to the more intense XRD diffraction peaks of $C_mN@H_2W_2O_7$ hybrids than those of the corresponding $C_mN@H_2WO_4$ hybrids.

### 3.6. Thermal analysis of the hybrids derived from $H_2WO_4$ and $H_2W_2O_7$ powders

Typical TG–DTA curves of the inorganic–organic hybrid compound of $C_8N@H_2WO_4$ are shown in Fig. 6. As the figure shows, the curves can be divided into 4 regions: (I) room temperature –170 °C, (II) 170–280 °C, (III) 280–410 °C and (IV) 410–600 °C. In region I, there are an obvious mass loss of ~29% and an intense endothermic peak at 150 °C, due to desorption of $n$-octylamine molecules. In region II, one can find a mass loss of 11% and a weak endothermic peak at 230 °C, which is due to desorption of structural water from the inorganic layers, besides due to the desorption of some $n$-octylamine molecules (ions) from the inner spaces of the lamel-

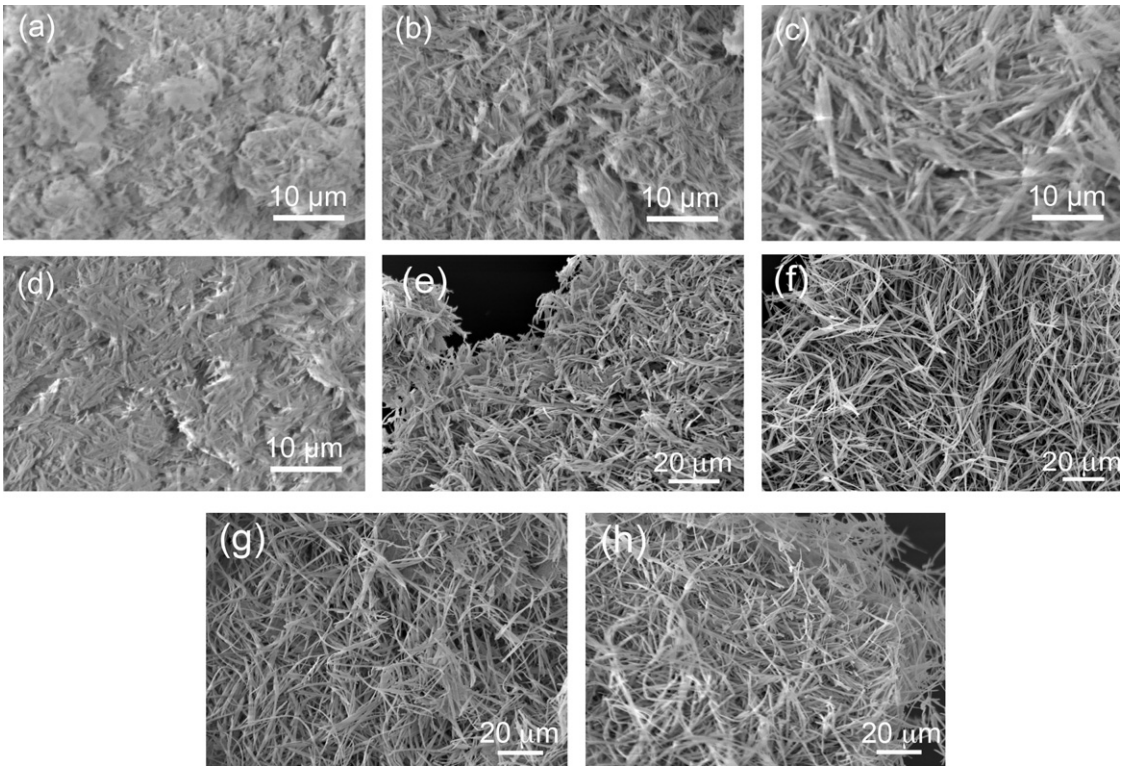


**Fig. 5.** (a–d) SEM images of the as-obtained $C_mN@H_2WO_4$ hybrids: (a) $m = 4$, (b) $m = 6$, (c) $m = 8$, and (d) $m = 10$; (e–h) SEM images of the as-obtained $C_mN@H_2W_2O_7$ hybrids: (e) $m = 4$, (f) $m = 6$, (g) $m = 8$ and (h) $m = 10$.

lar structures of $C_8N@H_2WO_4$. We can find an exothermic peak at 350 °C and a corresponding mass loss of 7% in region IV, and the exothermic peak and its corresponding mass loss are probably due to the oxidation of the residual *n*-octylamine molecules (ions). The intense exothermic peak at 480 °C and the corresponding mass loss of 6% in region IV can be assigned to the combustion of the residual carbon derived from the oxidation of the organic *n*-octylamine molecules (ions). When the temperature is higher than 600 °C, there are no obvious peaks either in the TG curve or in the DTA curve, indicating no change occurs after 600 °C. The other samples of $C_mN@H_2WO_4$ and $C_mN@H_2W_2O_7$ hybrids show similar DTA curves during the heating treatment from room temperature to 800 °C.

Fig. 7a shows the TG curves of the $C_mN@H_2WO_4$ hybrid compounds. As Fig. 7a shows, these TG curves take on similar profiles, which suggest that the compounds of $C_4N@H_2WO_4$, $C_6N@H_2WO_4$, $C_8N@H_2WO_4$ and $C_{10}N@H_2WO_4$ undergo a similar thermal decomposition process. The total mass losses increase from 37.6%, 46.7%, 52.8% and 61.0% for $C_4N@H_2WO_4$, $C_6N@H_2WO_4$, $C_8N@H_2WO_4$ and $C_{10}N@H_2WO_4$, respectively. Fig. 7b shows the TG curves of the $C_mN@H_2W_2O_7$ hybrid compounds. The total mass losses of $C_4N@H_2W_2O_7$, $C_6N@H_2W_2O_7$, $C_8N@H_2W_2O_7$ and $C_{10}N@H_2W_2O_7$ are 37.5%, 43.7%, 51.6% and 61.2%, respectively. When comparing Fig. 7a and b, one can readily find that the TG curves of the $C_mN@H_2W_2O_7$ compounds are very similar to those of the corresponding $C_mN@H_2WO_4$ compounds ($m = 4$, 6, 8 and 10), not only in the profiles of the TG curves but also in the data of the total mass losses between room temperature and 600 °C. The similarity in the profiles of the TG curves and the data of the total mass losses suggests the similarity in the compositions and microstructures between the $C_mN@H_2WO_4$ and $C_mN@H_2W_2O_7$ compounds.

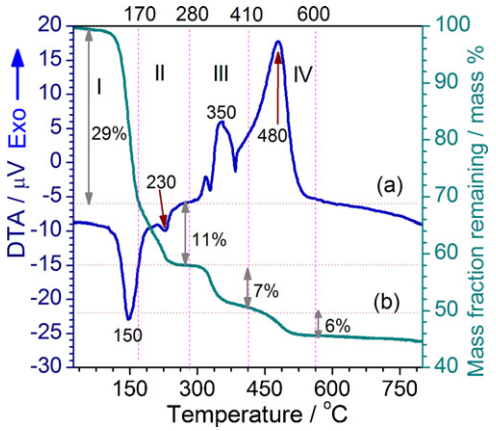


**Fig. 6.** TG–DTA curve of the $C_8N@H_2WO_4$ hybrid compound.

We suppose that the compositions of the tungstate-based inorganic–organic hybrids can be denoted as $(C_4H_9NH_3)_2WO_4$, $(C_6H_{13}NH_3)_2WO_4$, $(C_8H_{17}NH_3)_2WO_4$, $(C_{10}H_{21}NH_3)_2WO_4$, respectively, and that the resultant products are the $WO_3$ phase when the tungstate-based inorganic–organic hybrids are calcined at temperatures higher than 600 °C. The theoretical mass losses of the tungstate-based inorganic–organic hybrids are then calculated to be 41.5%, 48.7%, 54.4% and 58.9% for $C_4N$, $C_6N$, $C_8N$ and $C_{10}N$, respectively. These theoretical values are close to the corresponding experimental data not only for $C_mN@H_2WO_4$ compounds but also for $C_mN@H_2W_2O_7$ compounds. These TG results indicate that the chemical compositions of $C_mN@H_2WO_4$ hybrids and $C_mN@H_2W_2O_7$ hybrids are close to $(C_mH_{2m+1}NH_3)_2WO_4$ ($m = 4$, 6, 8 and 10).

### 3.7. Comparative analysis of the reactions of $H_2WO_4$ and $H_2W_2O_7$ powders with n-alkylamines

Both $H_2WO_4$ and $H_2W_2O_7$ powders can react with *n*-alkylamines in reverse-microemulsion-like media to form tungstate-based inorganic–organic hybrid compounds. The as-obtained

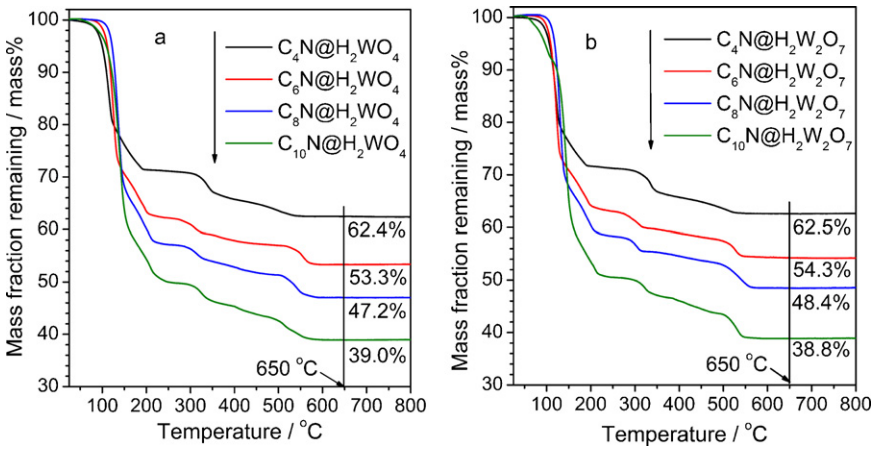


**Fig. 7.** TG curves of (a) $C_mN@H_2WO_4$ and (b) $C_mN@H_2W_2O_7$ hybrid compounds with $m = 4$, 6, 8 and 10.

$C_mN@H_2WO_4$ and $C_mN@H_2W_2O_7$ ($m = 4$, 6, 8 and 10) compounds are of similar characteristics in XRD patterns (Figs. 2 and 4), FT-IR spectra (Fig. S3) and TG–DTA curves (Fig. 7). Such similarities from various aspects make us safely conclude that the compounds of $C_mN@H_2WO_4$ and $C_mN@H_2W_2O_7$ ($m = 4$, 6, 8 and 10) are of similarities both in compositions and in microstructures, that is, both $C_mN@H_2WO_4$ and $C_mN@H_2W_2O_7$ are tungstate-based inorganic–organic hybrid compounds with a highly ordered lamellar structure, constructed by alternately stacking *n*-alkylammonium bilayers and single-octahedral W–O layers [27].

The morphology and microstructure of the $H_2WO_4$ powders used (Fig. S2a) are very different from those of the $H_2W_2O_7{\cdot}xH_2O$ powders (Fig. S2b), whereas the products obtained by treating them with *n*-alkylamines are very similar not only in morphology but also in composition. The results indicate that the reactions of $H_2WO_4$ and $H_2W_2O_7{\cdot}xH_2O$ powders with *n*-alkylamines undergo a similar process.

### 3.8. Formation mechanisms for hybrids derived from $H_2WO_4$ and $H_2W_2O_7$ powders

$H_2WO_4$ and $H_2W_2O_7{\cdot}xH_2O$ can be seen as solid acids, which can react with strong bases, forming water-soluble salts. But in the present work, a nonpolar reagent of heptane is used as the solvent. The reaction media of "tungstic acids/*n*-alkylamines/heptane" can be seen as pseudo "water-in-oil" microemulsions, wherein excess *n*-alkylamine molecules act as surfactants [27]. For $H_2WO_4$ powders with single W–O octahedral layers, the *n*-alkylamine molecules ($RNH_2$) react with $H_2WO_4$ particles via a proton-exchange process, forming $[RNH_3^+–WO_4^{2-}–^+H_3NR]$ species, each of which has a hydrophilic radical and two hydrophobic ones. The above stage can be seen as a dissolution process. These $[RNH_3^+–WO_4^{2-}–^+H_3NR]$ species can be reorganized in the nonpolar solvent due to the end hydrophobic radicals (R). To minimize the energy of the system, the $[RNH_3^+–WO_4^{2-}–^+H_3NR]$ species then spontaneously assemble to be a layered structure with an apparent morphology of nanobelts.

For $H_2W_2O_7{\cdot}xH_2O$ powders, there are double W–O octahedral layers. An intercalation process is undergone during the initial stage of their reactions with *n*-alkylamine molecules [27]. Upon intercalation of *n*-alkylamines, the crystal water molecules are released to form microscale water pools with a high alkalinity due to hydrolyzation of the excess *n*-alkylamine molecules. The double W–O octahedral layers of the intercalation products are then dissolved in the alkaline water pools to form $[RNH_3^+–WO_4^{2-}–^+H_3NR]$ species with single W–O octahedral layers. Similar to the case of $H_2WO_4$, the as-obtained $[RNH_3^+–WO_4^{2-}–^+H_3NR]$ species assemble to layered nanobelts. The dissolution of the double W–O octahedral layers during the reaction of $H_2W_2O_7{\cdot}xH_2O$ and *n*-alkylamines is supported by the high similarities between the final hybrid compounds from $H_2W_2O_7{\cdot}xH_2O$ and those from $H_2WO_4$, which is also supported by the intermediate products and the directly TEM observations [27]. The formation mechanisms for the tungstate-based inorganic–organic hybrid nanobelts using $H_2WO_4$ and $H_2W_2O_7{\cdot}xH_2O$ as the starting materials, respectively, can be described using the route chart shown in Fig. 1.

## 4. Conclusions

We have comparatively investigated the reaction behaviors of commercially available $H_2WO_4$ and $H_2W_2O_7{\cdot}xH_2O$ powders with *n*-alkylamines in reverse-microemulsion-like reaction media, *i.e.*, inorganic particles/*n*-alkylamines/heptane. $H_2WO_4$ powders reacting with *n*-alkylamines at room temperature led to the formation of inorganic–organic hybrid one-dimensional nanobelts, consisting of organic *n*-alkylammonium ions (a bilayer arrangement with a tilt angle of 65°) and inorganic single-octahedral W–O layers. The inorganic–organic hybrid nanobelts obtained from $H_2W_2O_7{\cdot}xH_2O$ powders were also took on a bilayered *n*-alkyl arrangement with a tilt angle of 74° along the single-octahedral W–O layers. The similarities in composition and microstructure demonstrated that the reactions of $H_2WO_4$ and $H_2W_2O_7{\cdot}xH_2O$ powders with *n*-alkylamines underwent a similar "dissolution–reorganization" process, where the double-octahedral W–O layers from $H_2W_2O_7{\cdot}xH_2O$ particles were firstly decomposed and the decomposed species were then reorganized into ordered lamellar hybrid nanobelts with inorganic single-octahedral W–O layers. This work provides a new and inexpensive route to synthesize tungstate-based inorganic–organic hybrid nanobelts, besides giving a novel convincing evidence for clarifying the reaction mechanism of $H_2W_2O_7{\cdot}xH_2O$ with *n*-alkylamines.

## Acknowledgements

This work was supported by the National Natural Science Foundation of China (No. 50802090), the China Postdoctoral Science Foundation (No. 20090450094), the Opening Project of State Key Laboratory of High Performance Ceramics and Superfine Microstructure (No. SKL200905SIC) and the Introduced Talent Project of Zhengzhou University. D. Chen thanks Professor Yoshiyuki Sugahara (Waseda University) for his valuable discussion on the formation mechanism of the tungstate-based inorganic–organic hybrid nanobelts.

## Appendix A. Supplementary data

Supplementary data associated with this article can be found, in the online version, at doi:10.1016/j.matchemphys.2010.09.039.

## References


[1] C. Sanchez, G.J.A.A. Soler-Illia, F. Ribot, T. Lalot, C.R. Mayer, V. Cabuil, Chem. Mater. 13 (2001) 3061.
[2] K. Ohtsuka, Chem. Mater. 9 (1997) 2039.
[3] C.S. Triantafillidis, P.C. LeBaron, T.J. Pinnavaia, Chem. Mater. 14 (2002) 4088.
[4] J. Livage, New J. Chem. 25 (2001) 1.
[5] J. Rouxel, M. Tournoux, Solid State Ionics 84 (1996) 141.
[6] M.R. Gao, W.T. Yao, H.B. Yao, S.H. Yu, J. Am. Chem. Soc. 131 (2009) 7486.
[7] K.N. Rao, L.D. Dingwall, P.L. Gai, A.F. Lee, S.J. Tavener, N.A. Young, K. Wilson, J. Mater. Chem. 18 (2008) 868.
[8] M. Ogawa, S. Okutomo, K. Kuroda, J. Am. Chem. Soc. 120 (1998) 7361.
[9] Z. Zhong, W. Ding, W. Hou, Y. Chen, X. Chen, Y. Zhu, N. Min, Chem. Mater. 13 (2001) 538.
[10] M.G. Kanatzidis, A.C. Sutorik, Prog. Inorg. Chem. 43 (1995) 151.
[11] M.G. Kanatzidis, C.G. Wu, H.O. Marcy, C.R. Kannewurf, J. Am. Chem. Soc. 111 (1989) 4139.
[12] A. Yamagishi, J. Phys. Chem. 86 (1982) 2472.
[13] M. Ogawa, K. Kuroda, Chem. Rev. 95 (1995) 399.
[14] Z.G. Zhao, M. Miyauchi, Chem. Commun. (2009) 2204.
[15] J.W. Zhao, J.L. Li, P.T. Ma, J.P. Wang, J.Y. Niu, Inorg. Chem. Commun. 12 (2009) 450.
[16] A. Tiwari, S.J. Li, Polym. J. 41 (2009) 726.
[17] E. Zelazowska, E. Rysiakiewicz-Pasek, J. Non-Cryst. Solids 354 (2008) 4500.
[18] S.P. Pang, F.F. Jian, L. Wang, Inorg. Chem. 47 (2008) 344.
[19] Q.S. Gao, C.X. Zhang, S.H. Xie, W.M. Hua, Y.H. Zhang, N. Ren, H.L. Xu, Y. Tang, Chem. Mater. 21 (2009) 5560.
[20] J.W. Johnson, A.J. Jacobson, S.M. Rich, J.F. Brody, J. Am. Chem. Soc. 103 (1981) 5246.
[21] A. Chemseddine, F. Babonneau, J. Livage, J. Non-Cryst. Solids 91 (1987) 271.
[22] B.S. Wang, Y.P. Li, X.W. Dong, X.N. Cai, Q.Y. Pan, W.M. Liu, Acta Chim. Sinica 67 (2009) 2199.
[23] B. Ingham, S.V. Chong, J.L. Tallon, Curr. Appl. Phys. 6 (2006) 553.
[24] M. Kudo, H. Ohkawa, W. Sugimoto, N. Kumada, Z. Liu, O. Terasaki, Y. Sugahara, Inorg. Chem. 42 (2003) 4479.
[25] R.E. Schaak, T.E. Mallouk, Chem. Commun. (2002) 706.
[26] B. Wang, X. Dong, Q. Pan, Z. Cheng, Y. Yang, J. Solid State Chem. 180 (2007) 1125.
[27] D. Chen, Y. Sugahara, Chem. Mater. 19 (2007) 1808.
[28] D. Chen, Y. Sugahara, Innov. Ceram. Sci. Eng. 352 (2007) 85.
[29] D. Chen, H. Wang, R. Zhang, S. Guan, H. Lu, H. Xu, D.Y. Yang, Y. Sugahara, L. Gao, Chem. J. Chin. Univ. 29 (2008) 1325.
[30] D. Chen, H. Wen, H. Chen, H. Wang, R. Zhang, H. Xu, D. Yang, H. Lu, Mater. Chem. Phys. 116 (2009) 507.
[31] D. Chen, L. Gao, A. Yasumori, K. Kuroda, Y. Sugahara, Small 4 (2008) 1813.
[32] D. Chen, X. Hou, H. Wen, Y. Wang, H. Wang, X. Li, R. Zhang, H. Lu, H. Xu, S. Guang, J. Sun, L. Gao, Nanotechnology 21 (2010) 035501.
[33] M.S. Whittingham, A.J. Jacobson (Eds.), Intercalation Chemistry, Academic Press, New York, 1982.
[34] G. Lagaly, Angew. Chem. Int. Ed. 15 (1976) 575.
[35] J.A. Dean (Ed.), Lange's Handbook of Chemistry, McGraw-Hill, New York, 1999.
[36] S.V. Chong, B. Ingham, J.L. Tallon, Curr. Appl. Phys. 4 (2004) 197.
[37] I.V. Chernyshova, K.H. Rao, A. Vidyadhar, A.V. Shchukarev, Langmuir 16 (2000) 8071.
[38] B. Ingham, S.V. Chong, J.L. Tallon, J. Phys. Chem. B 109 (2005) 4936.
[39] R.G. Nuzzo, E.M. Korenic, L.H. Dobois, J. Chem. Phys. 93 (1990) 767.
[40] S.H. Park, C.E. Lee, Chem. Mater. 18 (2006) 981.
[41] R.M. Silverstein, G.C. Basser, T.C. Morrill (Eds.), Spectrometric Identification of Organic Compounds, Willey, New York, 1991.